Properties of an ECWR Discharge at Low Pressures

Vladimir P. Sushkov, Severin A. Handelshauser, and Gerhard Franz

***Abstract*— We report an experimental study of an electron cyclotron wave resonance (ECWR) plasma source. The dimensions of the source are considerably larger than in similar experiments. The excitation frequency is 27.12 MHz, the working gas is argon at very low pressures below 0.13 Pa. Spectroscopic data connected with a global model yield electron temperature T_e, electron number density n_e, population of the metastable state n_m. The pressure dependencies of these quantities are discussed. Starting from $T_e \sim 5$ eV at pressure $p = 0.13$ Pa the temperature grows as the pressure goes down until the discharge extinguishes at $\sim 0.6 \times 10^{-2}$ Pa. It becomes in the meantime so high that the emission spectra feature strong Ar(II) lines in the region 400–500 nm. At $p = 0.13$ Pa and power 300 W the electron density on the axis is about 4×10^{10} cm^{-3} and falls down due to the increase in T_e as the pressure drops. The discharge was also electrically characterized to determine the plasma impedance Z. The impedance and the plasma resistance $\mathrm{Re}(Z)$ are presented as functions of the static magnetic field B_0. The distribution of power losses are also shown as B_0-dependencies.**

***Index Terms*— Discharge impedance, electron cyclotron wave resonance (ECWR), emission spectroscopy, weakly magnetized inductively coupled plasma (mICP).**

I. Introduction

ABSORPTION of electromagnetic waves is an efficient electron heating mechanism found in many kinds of high-density plasma sources. A static magnetic field B_0 is often used in such devices to enable wave propagation at frequencies below the plasma frequency ω_p. Thus, magnetically enhanced inductively coupled plasma (ICP) discharges in the radio frequency range are known to increase their efficiency and manifest resonancelike phenomena at certain B_0 values [1]–[5]. These values correspond to the electron cyclotron resonance $B_0 = B_c$ and to a further resonance at $B_0 = k \cdot B_c$, where factor $k > 1$ assumes a value around 2 or 3. This latter resonance is referred to by various terms including cavity, transmission, or right-hand polarized-wave resonance. It is caused by standing wave formation of the right-handed mode of the electron cyclotron wave, so this is also called the electron cyclotron wave resonance (ECWR) effect. A concise and clear introduction to this effect can be found in [6].

Manuscript received January 30, 2019; revised April 25, 2019; accepted June 11, 2019. Date of publication July 3, 2019; date of current version August 9, 2019. This work was supported by the Bavarian State Ministry of Science and Art under Project VIII.2-F1111.MÜ/21/3. The review of this paper was arranged by Senior Editor S. Portillo. *(Corresponding author: Vladimir P. Sushkov.)*

V. P. Sushkov and G. Franz are with the Department of Applied Sciences and Mechatronics, Munich University of Applied Sciences, 80335 Munich, Germany (e-mail: sushkov@hm.edu).

S. A. Handelshauser is with the Ludwig Maximilian University, 80539 Munich, Germany.

Color versions of one or more of the figures in this paper are available online at http://ieeexplore.ieee.org.

Digital Object Identifier 10.1109/TPS.2019.2923548

A dedicated type of ECWR plasma sources [7], [8] uses discharge configuration of special design, consisting of a glass cylinder and B_0 perpendicular to its symmetry axis. Such plasma sources exhibit a pronounced resonancelike increase in plasma density at the ECWR condition. From the electrotechnical point of view, the deeper penetration of the RF electric field enhances the plasma resistance $\mathrm{Re}(Z)$ which is the real part of the impedance. At the ECWR condition, a substantial electric field exists throughout the whole plasma volume, the resistance thereby has a maximum at this point while the plasma reactance $\mathrm{Im}(Z)$ drops. This leads to the most effective power transfer because the absorption of the wave energy is proportional to the plasma resistance. The absorbed power P_{abs} translates directly into the number of the created electron–ion pairs.

Another property of ECWR discharges, common with other magnetized discharges and attractive in many applications, is the ability to work at very low pressures going down to $\sim 10^{-2}$ Pa. However, in numerous studies dedicated to this type of discharge, very few results have been reported for pressures below 0.133 Pa (1 mTorr). The work by Crolly and Oechsner [9] is a remarkable exception in this regard. In a certain sense, the present study is an extension to the cited work [9]. We focus on the discharge behavior below 0.13 Pa when the electron temperature starts changing drastically.

A detailed description of the experimental setup is given in Section II. Our source is aimed at application for broad ribbon-like ion beam extraction and treatment of temperature-sensitive surfaces. Noninvasive diagnostics are needed to monitor and control the device. In Section III, we elaborate an approach that allows us to obtain electron density n_e, temperature T_e and excited states density from optical emission spectroscopy (OES) in combination with a simple modeling. A method of electrical characterization is also described. Although the geometry of the setup did not allow us to use a Langmuir probe for a crosscheck, independent techniques yield good agreement in n_e, giving confidence in the results presented in Section IV. Furthermore, in Section V, the results are put in the context of other ECWR studies, refinement and limitation of the global model are discussed. A brief summary is given in Section VI.

II. Experiment

Our plasma setup was individually manufactured by HS-Group GmbH (Hainburg, Germany). The whole vacuum vessel is made of stainless steel and consists of two parts: the plasma source and the processing chamber. The plasma source is a chamber with inner dimensions of 110 cm × 27.5 cm × 25 cm ($L \times W \times H$) containing a glass cylinder of inner radius $R = 11$ cm and length $L = 103$ cm. This cylinder is hanging on special dielectric suspenders to avoid contact with the

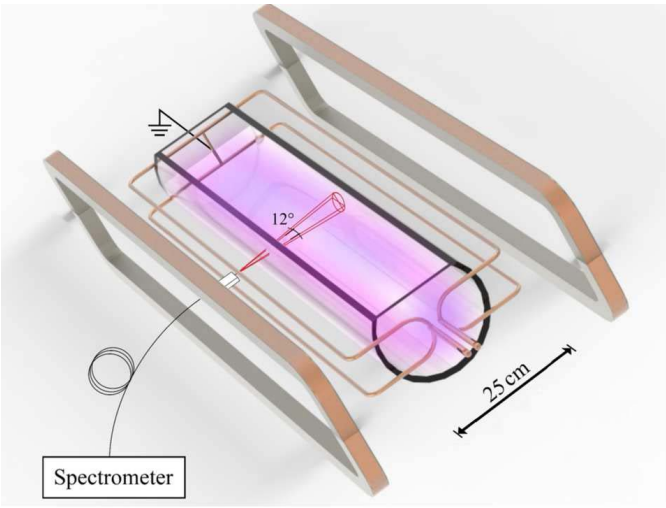

Fig. 1. 3-D representation of the plasma source geometry. The truncated glass cylinder is enfolded with the RF-antenna. Two rectangular magnetic coils enframe the discharge from the outside.

chamber walls. Going along the cylinder there is an induction coil of tubular copper with water cooling in it. In effect, this is an RF-antenna, used for plasma excitation at driving frequency $f_0 = 27.12$ MHz. A steady magnetic field up to 5×10^{-3} T was created in the plasma source by two rectangular coils 130 cm × 25 cm ($L \times W$) placed outside the vacuum vessel. The two coils set in a Helmholtz-like arrangement with a separation of 40 cm allowed a fairly uniform magnetic field across the axis of the glass cylinder. They were driven by a dc current source, whereby a current of 1 A induces a 5×10^{-4}-T magnetic flux density in the middle.

The described spatial configuration of the plasma source is displayed in Fig. 1. The RF antenna is of a single loop type, although it may misguidedly appear more complex due to the doubled arms. The antenna was connected to ground at the point opposite to the feed ports. This in combination with symmetrical drive ensures the reduction of the RF potential with respect to the ground along the antenna and thus the unwanted RF potential in the plasma. Also, it is seen in Fig. 1 that the glass cylinder was actually truncated at 3/4 of its height. The resulting opening was covered with steel plates having 4-mm slits in the middle. There was a possibility to electrostatically manipulate the effluent ion flux, which was not exploited in the present study. These slits connected the plasma source with the processing chamber, a voluminous vessel (130 cm × 64 cm × 64 cm) built above the plasma source. The entire vacuum system was electrically grounded. It was pumped down to a residual pressure of $\sim 10^{-5}$ Pa by a turbomolecular pump (Pfeiffer TPH 2200, nominal pumping speed 2200 l/s) backed by a rotary vane pump. The working gas (argon) was fed directly into the glass cylinder. Since the pumping port is located in the wall of the processing chamber, there was a difference in pressure by a factor of 1.5–2 between the plasma source and the processing chamber due to significant flow resistance. A CMR 361 Baratron (Pfeiffer Vacuum) was used to monitor the working gas pressure in the plasma source, which was varied by changing the mass flow. The series of measurements reported here were performed in the pressure range 0.008–0.12 Pa, close to the lower pressure limit of sustained discharge.

The antenna was powered by an RF generator Dressler HPG 2575 [Dressler HF-Technik GmbH, Stolberg (Rhld.), Germany]. In our experiments, the output powers reached up to 1000 W. Higher applied powers could bring damage to the matching unit, especially at the lowest pressures. Attached to the antenna, the matching unit is based on an air-core transformer and two adjustable capacitors contained in an aluminum box. The functional principle is the same as that of a balun device, matching the impedances and allowing the symmetrical drive of the antenna.

A sensor V(I)-Probe-4100 (MKS Instruments, Inc., Andover, MA, USA) for reading the RF current and voltage was placed in circuit between the generator and the matching box, the circuit diagram is shown in Fig. 2. The sensor is in principle a two-port with four gates, which contains transducers for current and voltage. It is designed not to disturb key process parameters and to remove influences of the hostile conditions in the current path on their measurements [10]. From this extremely carefully designed housing, shielded cables transmit the current and voltage signals to an oscilloscope. The resulting waveforms were then sampled and stored by Tektronix TDS1001B digital oscilloscope. These signals have been analyzed in terms of fundamental harmonics and a phase shift between them, which allowed determination of such key discharge parameters as the impedance, the resistance, and the absorbed power.

For the purpose of plasma diagnostics, a grating spectrometer OMA III (EG & G Princeton Applied Research, Woburn, MA, USA) was employed to perform optical emission spectroscopy in the visible range. An intensified diode array (1455R-700-HQ, EG & G Princeton Applied Research) was used for signal detection. The spectrometer has optionally three gratings of 150, 600, and 1200 lines/mm in Czerny–Turner arrangement, the one with 600 mm/lines having been used for most of the measurements. This gives ∼100-nm bandwidth of a single scan with a spectral resolution of about 0.3 nm. The communication to the PC was realized by a self-developed LabView program, permitting a time resolution of approximately 40 s for a single recording. The light signal was fed by a bundle of four optical fibers. Its end was placed adjacent to a viewing port in the middle of the plasma source. The optical fiber accepted light within a cone with an opening angle of ∼12°.

III. Diagnostics

Much valuable information on discharge can be obtained through analysis of its emission spectra. Within the scope of this study, we are interested in quantities like electron temperature T_e, electron number density n_e, and the number densities n_m and n_r of $1s_5$ metastable and $1s_4$ resonance states, respectively. Using the optical emission cross sections within our line ratio method implies *the corona model* for the population of the excited/ionized states. An *a priori* applicability

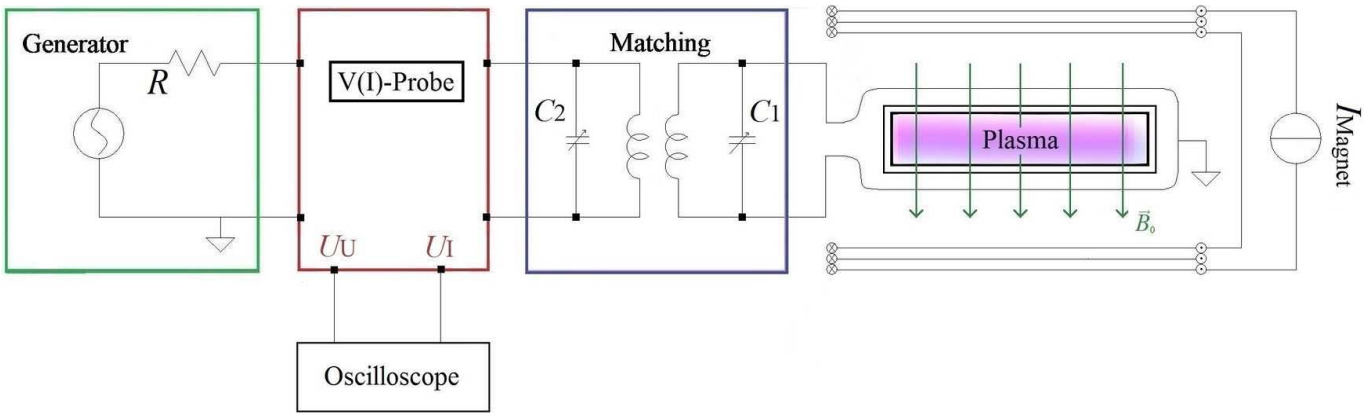

Fig. 2. Circuit diagram for the RF power transmission.

of the model might be questioned [11] at the ionization degree in the range 0.001–0.01 relevant for the plasma source. It can be shown, however, that the kinetics of the selected lines at our relatively high T_e meets the assumptions of the model.

A. Electron Temperature

The electron temperature T_e was determined from the charged particle balance of the plasma source. In order to validate the resulting $T_e(p)$, it was used to calculate ratios of spectral lines which were then compared with those obtained from the experiment.

In the frame of the charged particle balance model, the surface particle loss is equated to the volume ionization, yielding [12]

$$\frac{k_{\text{ion}}(T_e)}{u_B(T_e)} = \frac{1}{n_g d_{\text{eff}}} \tag{1}$$

with k_{ion} being the rate constant for ionization, u_B is the Bohm velocity, n_g is the ground state number density, and d_{eff} is the effective plasma size. When the plasma source has volume V and particle loss surface S, the effective plasma size can be calculated as

$$d_{\text{eff}} = \frac{V}{S} \tag{2}$$

which was $d_{\text{eff}} = 5$ cm for our plasma source. The losses due to the volume recombination are left out because of a relatively low ionization degree in promille region and a high temperature. The ionization cross section, which is needed to evaluate k_{ion}, was taken from [13]. The resulting temperature curve is shown in Fig. 5(a).

Excitation of a spectral line is described by the *optical emission* cross section σ_{opt}, which is the *apparent* cross section times the branching ratio of the line of interest. The energy and pressure dependent cross sections $\sigma_{\text{opt}}(E, p)$ for argon lines are tabulated in [14]. The cross sections given there were integrated in the required way to yield the rate constants $k_{\text{opt}}(T_e, p) = \langle \sigma_{\text{opt}} \upsilon \rangle$, under the assumption of a Maxwellian electron velocity distribution. The *line intensity* I depends on plasma parameters as follows:

$$I \sim n_e n_g k_{\text{opt}}(T_e, p) \tag{3}$$

where n_e and n_g are the number densities of the electrons and the ground state atoms, respectively.

A ratio of two lines $r = I_1/I_2 = k_{\text{opt1}}/k_{\text{opt2}}$ can be used to monitor the electron temperature as long as it is sensitive to T_e variation at the working conditions. Since our spectrometer has a nonuniform spectral response, we deal with the relative variations of the ratios.

We used two spectral ranges: "blue" 420–520 nm and "red" 680–780 nm, taken at the same discharge conditions. The emission spectra in the blue range featured argon ion lines [see Fig. 3(a)]. These lines belong to the transition array $3p^4 4s - 3p^4 4p$ of Ar^+. They are quite well observable at the lowest pressures ~0.01 Pa and decrease to zero toward $p \sim 0.1$ Pa. Stronger ion lines were selected for the analysis, these are the five lines indicated in Fig. 3(a).

All the Ar(I) lines which we evaluated in the blue range 420–520 nm have roughly the same course, like do all the Ar(II) lines. Their behavior is illustrated in Fig. 3(b), which showcases representative pressure dependences of an ion line intensity, a neutral line, and their ratio. The *line intensity* is the area of the spectral line obtained from a fit. It was a Gauss fit when the line was well isolated from the neighboring lines. However, often there was a need to treat groups of two to three lines which were not completely resolved. It was necessary to apply Voigt fit which gives more reliable results in this case.

Five ion/neutral line ratios have been evaluated, each Ar(II) line relating to a different Ar(I) line. Since all these ratios exhibit very similar T_e-dependence, we employed lines from the red region 680–780 nm to form line ratios of different T_e-dependence.

We found that the line at 720.7 nm has a more distinct and stronger dependence than the other intense lines, see the inset plot in Fig. 4. The behavior of the optical excitation rate constants of 693.77- or 703.03-nm lines is typical for the most observed lines in this spectral region, while the 720.7-nm line has a more persistent growth at higher temperatures. The peculiarity of this line is that its higher level—$3s_2$ in Paschen notation—is a resonant one, i.e., has a dipole allowed the transition to the ground state. As a consequence [14], its optical excitation cross section features a broad maximum at ≈ 90 eV, while the other excitation functions have sharper maxima at

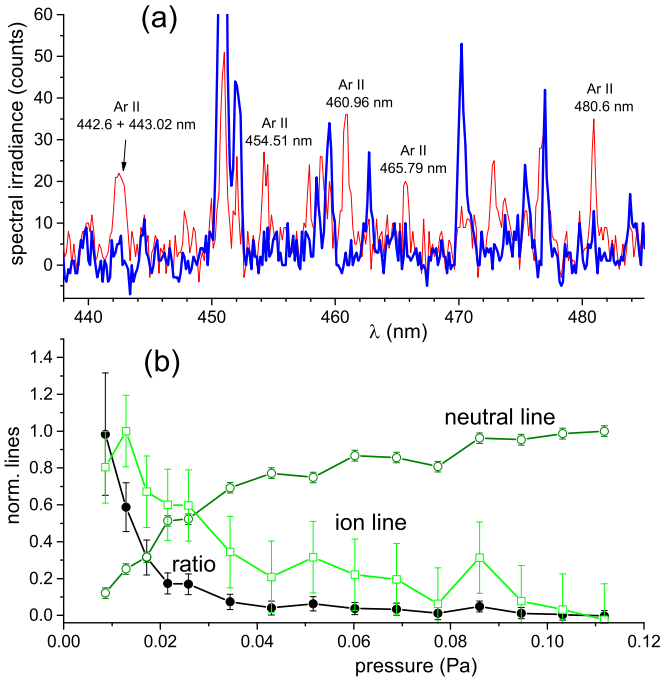

Fig. 3. Argon spectra in the blue spectral region featuring ion lines, at ECWR resonance and $P_{gen} = 300$ W. (a) Two overlayed emission spectra at different pressures, 0.017 Pa (red thin line) and 0.1 Pa (blue thick line). (b) Pressure dependence of Ar(I) 451.07 nm and Ar(II) 454.5 nm lines and their ratio, normalized to unity at the maxima.

TABLE I
LINE RATIOS USED IN THIS STUDY

ratio	Ar(II) [nm]	levels	Ar(I) [nm]	levels
r_1	442*		452.23	$1s_3$–$3p_{10}$
r_2	454.51	$4s\,^2P_{3/2} - 4p\,^2P^o_{3/2}$	451.07	$1s_2$–$3p_5$
r_3	460.96	$4s'\,^2D_{5/2} - 4p'\,^2F^o_{7/2}$	433**	
r_4	465.79	$4s\,^2P_{3/2} - 4p\,^2P^o_{1/2}$	430.01	$1s_4$–$3p_8$
r_5	480.60	$4s\,^4P_{5/2} - 4p\,^4P^o_{5/2}$	470.23	$1s_2$–$3p_{10}$
	Ar(I)		Ar(I)	
r_6	720.70	$2p_3$–$3s_2$	693.77	$2p_{10}$–$4d_6$
r_7	703.03	$2p_9$–$3s_5$	693.77	$2p_{10}$–$4d_6$
r_8	696.54	$1s_5$–$2p_2$	727.29	$1s_4$–$2p_2$
r_9	706.72	$1s_5$–$2p_3$	738.40	$1s_4$–$2p_3$

* 442 = 442.6 ($4s^4P_{3/2} - 4p\,^4D^o_{5/2}$) + 443.02 ($4s^4D_{1/2} - 4p\,^4D^o_{3/2}$)
** 433 = 433.36 ($1s_2$–$3p_3$) + 433.53 ($1s_2$–$3p_2$)

~ 20 eV with a rapid decrease at higher energies. This results in the calculated optical rates and their ratios shown in Fig. 4. The three plotted ratios with different T_e-dependencies have been used to validate the obtained temperature curve.

Table I contains the detailed information on the nine line ratios $r_i (i = 1, \ldots, 9)$ used in this paper. The nominator of a ratio is described in columns 2 and 3, the denominator in columns 4 and 5. Seven ratios r_1–r_7 have been used for T_e and n_e diagnostics, r_8 and r_9 for determination of the excited

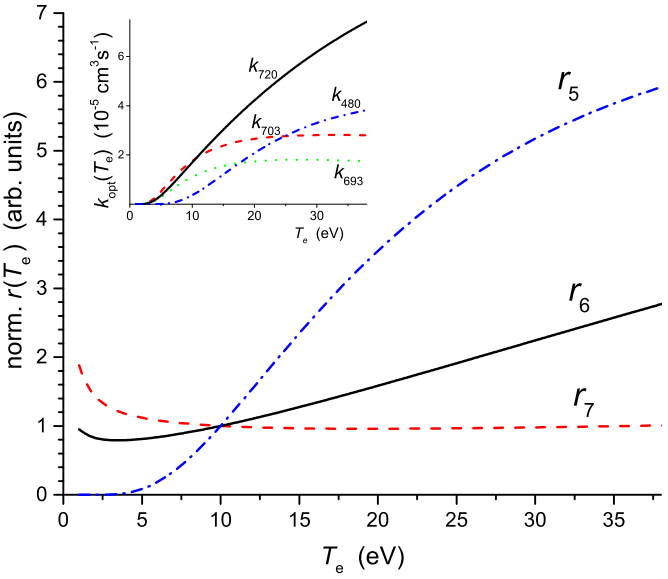

Fig. 4. Rate constants of spectral line excitation calculated with data from [14] (inset) and their ratios. The ratios are normalized to their values at $T_e = 10$ eV.

states' density addressed in this section later. Two unresolved spectral lines, which are supplied with footnotes, have been used due to very similar T_e- and p-dependencies of their components.

In contrast to the cross sections of direct excitation, which by definition do not depend on target gas density, the optical emission cross sections do include pressure dependence. The reason is the influence of resonance states and trapping of the radiation occurring on the resonant lines. In order to remove this pressure dependence from the experiment data, pressure p have been first recalculated according to $p_{eff} = (R/R')p$, where $R = 11$ cm and $R' = 1.4$ cm correspond to the cylindrical geometry of this paper and that of [14]. Then, the measured line intensities have been divided by the coefficients given in Tables II and III of [14]. After doing this, the line intensities are described by excitation rate constants which are functions of T_e alone.

It is not that every excited state has significant pressure dependence. In some cases, it can be neglected. Thus, 693.77- and 703.03-nm spectral lines need not be corrected, whereas 720.7-nm line has very strong pressure dependence due to a resonance state as the upper level. Most of the red lines originating from $2p$-manifold tend to have strong pressure dependencies. They also might be influenced by self-absorption and by excitation from the metastable state, so we avoid using them for T_e validation. In the blue region, line 451.07 nm and the composite line 433 nm must be pressure corrected. Ion lines generally do not need corrections.

The modeled and experimental line ratios are compared in Fig. 5(b) and (c).

B. Plasma Density

The relative course of electron number density have been obtained from (3) directly, without making line ratios. In case

of pressure variation, this cannot be done in a straightforward manner, because an additional data processing was necessary to remove the p- and T_e-dependencies of the emission lines. The latter was done using the obtained temperature curve and the optical rate constants $k_{opt}(T_e, p)$.

Absolute values of n_e can be estimated in two different ways. First, we take the condition for the s-order resonance in a plasma slab l (see [15])

$$\frac{(2s+1)\pi}{l} = \frac{\omega_{pe}}{c\sqrt{\omega_c/\omega - 1}} \tag{4}$$

where $\omega_c = eB_0/m_e c$ is the cyclotron angular frequency and ω_{pe} is the plasma frequency. From this, we can calculate plasma density n_e for the fundamental mode $s = 0$

$$n_e = \frac{m_e \epsilon_0}{e^2}\left(\frac{\pi c}{l}\right)^2\left(\frac{\omega_c}{\omega} - 1\right). \tag{5}$$

The model behind this expression is rather simple. It can be modified to include the effects of plasma nonuniformity (parameter q), the effects of the circular plasma cross section (parameter t, $l = 2R \cdot 2/\pi$), and the *warm plasma* effect [7]. The latter is accounted for by an additional term in the denominator which is proportional to T_e

$$n_e = \frac{m_e \epsilon_0}{e^2}\left(\frac{q\pi c}{l}\right)^2 \frac{\beta - t}{1 + t(\beta - t)^{-2} q^2 (\pi/l)^2 k T_e/(m_e \omega^2)}. \tag{6}$$

Here, $\beta = \omega_c/\omega$ is a standard designation. Given the magnetic field B_0, we can calculate the plasma density. This expression is meant to return values on the axis at their maximum.

The second way to estimate n_e is from the global model by using the power balance[12, eq. (10.2.5)]

$$n_e = \frac{P_{abs}}{e u_B S \mathcal{E}_T}. \tag{7}$$

Here, u_B is the Bohm velocity and $\mathcal{E}_T(T_e)$ is the ionization cost per ion–electron pair created. P_{abs} is the absorbed electromagnetic power. At resonance, generator power P_{gen} is almost entirely absorbed in the plasma.

C. Excited States' Density

Each spectral line is subjected to self-absorption when the optical density is not negligibly small. This effect depends on the population of the lower state and can be used to determine it [16], [17]. The degree of self-absorption is given by *escape factor* θ, $0 < \theta < 1$. It can be obtained from line ratios, when both lines of a ratio originate from the same upper level. The line ratio in an optically thin case $(I_1/I_2)_{ref}$ depends on the transition probabilities and the spectral sensitivity of the spectrometer. When $(I_1/I_2)_{ref}$ is known, the escape factors can be determined from the measured ratio $(I_1/I_2)_{mes}$ according to

$$\frac{\theta_1}{\theta_2} = \frac{\left(\frac{I_1}{I_2}\right)_{mes}}{\left(\frac{I_1}{I_2}\right)_{ref}}. \tag{8}$$

We chose two line ratios within the "red" spectral region: $r_8 = 696.54/727.29$ and $r_9 = 706.72/738.4$ with $2p_2$ and $2p_3$ as the upper state, respectively. The lower states were $1s_5$ and $1s_4$ in each case. The relation between θ and the number density of the lower state n_1 is given by

$$\theta = \frac{1}{1 + 2R\sigma_0 n_1} \tag{9}$$

where σ_0 is the optical absorption cross section in the line center, and $\tau = 2R\sigma_0 n_1$ is the optical thickness over $2R$ plasma extention. After the ratios of escape factors (8) are determined from the experiment, it remains to solve a system of two linear equations in order to obtain the densities of s_5 and s_4 states. An argon-filled Pen-Ray 90-0013-01 lamp was used as an optically thin spectral source for determination of $(I_1/I_2)_{ref}$.

D. Plasma Impedance

The V(I)-probe was located between the generator and the matching unit, Fig. 2. A direct measurement would thus yield the combined impedance of the matching unit and the discharge. To determine the impedance Z of the plasma alone, we needed to separate the contributions of the plasma load and the matching. To this end, the matching unit was modeled as a standard two-port network and then characterized for different settings of capacitors C_1 and C_2 in a special series of measurements. With the resulting matrix, we can recalculate the voltage and current measured on the primary side to obtain those on the secondary side at the antenna's terminals. With these values, we arrive at the impedance of the antenna loaded with plasma. We can also calculate the power absorbed in the matching unit. Further details are found in [18]. The primary concern in this paper was the resistance $\mathrm{Re}(Z)$ which determines the deposition of power in plasma.

IV. Results

A. Electron Temperature

The electron temperature as a function of the pressure is shown in Fig. 5(a). It is about 5 eV at higher pressures and rises ever more rapidly reaching the value of ~35 eV as the pressure approaches the lower limit. This is a straightforward result of solving (1). The presented temperature curve $T_e(p)$ was used in the calculation of the modeled line ratios. The experimental and modeled ion/neutral line ratios are plotted in Fig. 5(b). Only one modeled ratio r_5 is shown because the others are very similar to it. Two neutral/neutral ratios r_6 and r_7, both experimental and simulated, from the red spectral region are seen in Fig. 5(c).

B. Plasma Density

The relative variation of the plasma density with pressure is shown in Fig. 6(a). The three different methods of n_e determination were: spectroscopic data analysis with (3), the magnitude of the resonance magnetic field B_{res} and (6), and the absorbed power P_{abs} and (7). $T_e(p)$ needed at the input of all three procedures was already presented above. In the calculation from the magnetic field, the nonuniformity

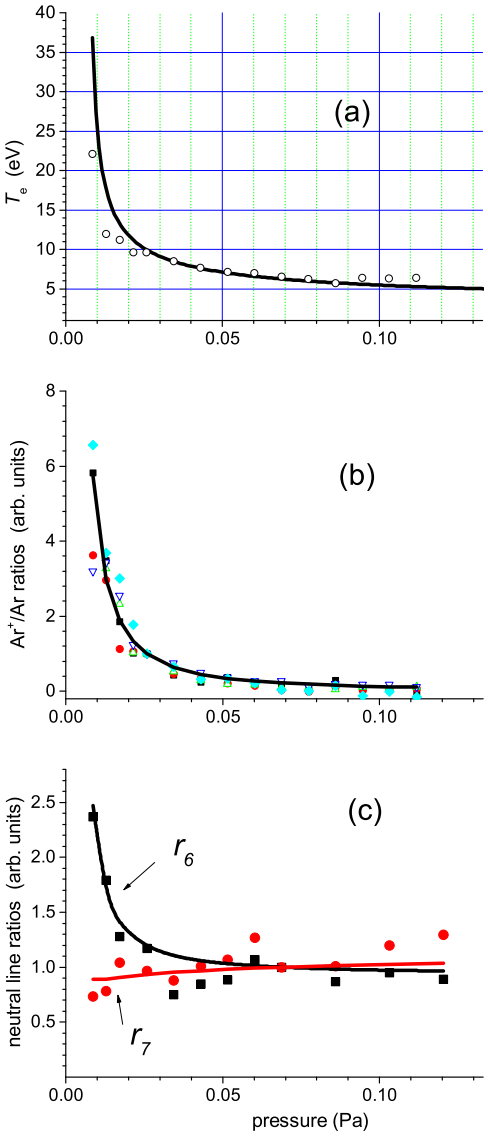

Fig. 5. Pressure dependencies of T_e and line ratios. (a) $T_e(p)$: solid line—resulting from the charged particles' balance, open circles—from [9] (see Discussions for explanations). (b) Ar(II)/Ar(I) line ratios r_i, $i = 1, \ldots, 5$ (refer to Table I). Experimental data were taken at the ECWR condition and $P_{gen} = 300$ W: r_1 (▽) r_2 (■), r_3 (◆), r_4 (●), r_5 (△). The full line represents the modeled r_5 ratio. All data sets are normalized to unity at a certain point. (c) r_6 und r_7 ratios from the red spectral region; experiment values are shown with symbols, the modeled ratios are plotted with lines.

parameter was assumed $q = 1.3$ and the cross-sectional parameter $t = 1.41$. The choice of q corresponds to an intermediate collisional regime of the ions, and the choice of t accounts for the plasma cross section which has equal dimensions parallel and perpendicular to the magnetic field. For a circular cross section, the plasma dimension l is assumed as $l = 2R \cdot 2/\pi$. These earlier theoretical estimates of the parameters [7] have been later confirmed by simulations in [19] (not for q though, because the plasma was modeled uniform). The absolute curves of the plasma density, calculated from B_{res} and from P_{abs}, are plotted in Fig. 6(b).Although their relative courses agree well, the absolute values differ by a factor of 3.5. This issue will be addressed later in Section V.

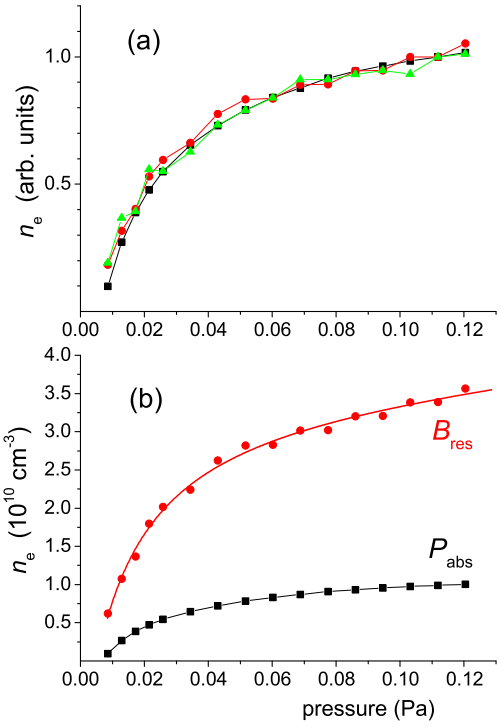

Fig. 6. Pressure dependence of the plasma density at the ECWR condition and $P_{gen} = 300$ W. (a) Relative course, calculated from the power balance (■), from B_{res} (●), and from the spectrosocopic data (▲). (b) Corresponding absolute values from the above-mentioned calculations.

C. Excited States

In the application of the technique described in Section III-C, the reference values $(I_1/I_2)_{ref}$ obtained in the optically thin case were: $r_8 = 5.4$ and $r_9 = 0.62$. Theoretical values for a perfectly flat spectral characteristic would be 3.5 and 0.45, respectively. The noise in the experimental data was the major issue with this technique because the derived metastable density is sensitive to it. In spite of the resulting scattering, the mean value would nicely reproduce the true value of the number density (see [20, Fig. 8]). The amount of our data points was not large enough for good statistics. Therefore, the data were averaged over different discharge powers at constant pressure, the outcome is shown in Fig. 7. The self-absorption of the lines ending on the resonance state $1s_4$ was not detectable in our case, so the escape factor was set $\theta = 1$ for these lines. Consequently, $1s_4$ density was not determined and $1s_5$ density was obtained from the two lines ending on the metastable state. Note that their escape factors must be very close to each other because the corresponding optical cross sections differ by mere 3% in magnitude. The number density of $1s_5$-state is about 10^{10} cm^{-3} throughout most of the pressure range and it gets about three times larger at the lowest pressure.

D. Plasma Impedance

The impedance of the discharge, resulting from the RF current and voltage on the secondary side, is presented in Fig. 8. This impedance is directly related to *the surface plasma impedance* [15]. The plot shows the magnitude $|Z|$ and the

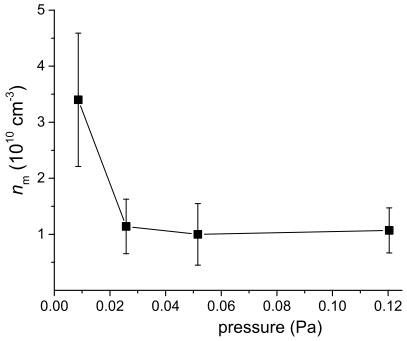

Fig. 7. Pressure dependence of the number density of metastable atoms.

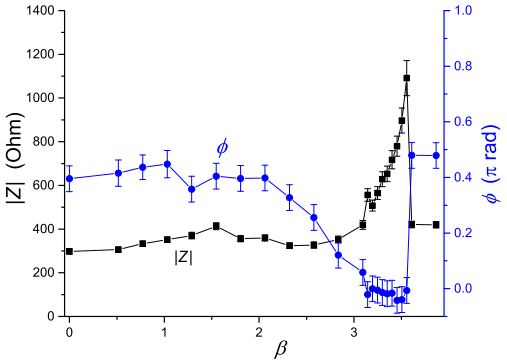

Fig. 8. Discharge impedance as function of the magnetic field, $\beta = B_0/B_c$, $B_c = 9.7 \times 10^{-4}$ T. $|Z|$ is given by squares and ϕ by circles. $P_{gen} = 500$ W and pressure $p = 86$ mP.

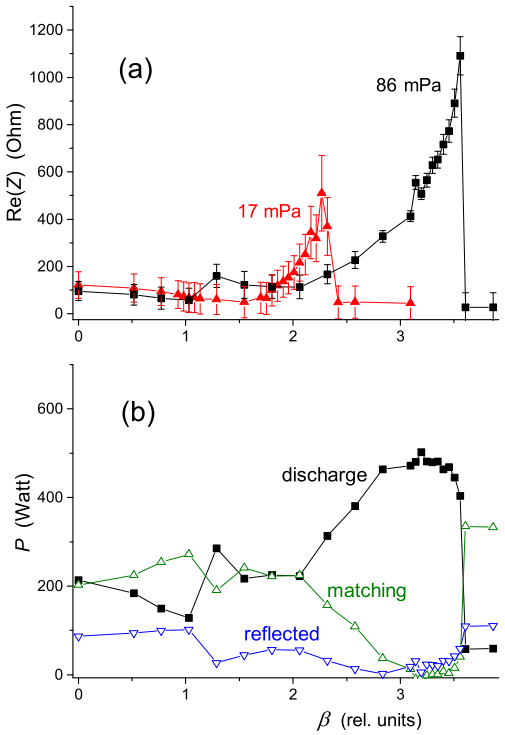

Fig. 9. Magnetic field dependencies of selected discharge characteristics at $P_{gen} = 500$ W, $\beta = B_0/9.7 \times 10^{-4}$[T]. (a) Plasma resistance for two different pressures $p = 0.017$ Pa (●) and $p = 0.086$ Pa (■). (b) Distribution of the total power at $p = 0.086$ Pa between the power absorbed in the discharge, in the matching box and the reflected power.

phase $\phi = \arg(Z)$ of this complex quantity as functions of the static magnetic field, taken at discharge pressure $p = 0.086$ P. The corresponding resistance $|Z|\cos(\phi)$ is given in Fig. 9(a) in full squares. The ECWR is quite prominent and the resistance rises about an order of magnitude at the maximum. The figure also features the resistance at a lower pressure $p = 0.017$ Pa, given in triangles. The difference in behavior is explained below in Section V. The total generated power was held constant $P_{gen} = 500$ W. The corresponding power absorption curves are plotted in Fig. 9(b). The settings of the matching unit, which was tuned for the optimal power transfer at the ECWR, were kept constant during the measurement. Outside the resonance, the power transmission to the discharge was less efficient. The rest of the power was reflected some extent but mostly lost in the matching box. Generally, the properties of the discharge display a sort of hysteresis at varying magnetic field, i.e., they depend on the direction of a B_0-scan. The corresponding shift is by 2×10^{-4} T downward when a measurement is repeated from high to low B_0. For the results presented, the direction of B_0-scan was from low to high values.

V. Discussion

Electron temperatures at the reference pressure of 0.133 Pa (1 mTorr) of argon, typical for ECWR experiments, range from 4 to 10 eV [3], [6]–[9], [21], [22]. The value of the present study $T_e(0.133\ \text{Pa}) = 5$ eV is consistent with these data. Furthermore, T_e should tend to lower values in our case because of the high-aspect plasma source which has a larger d_{eff}. At extremely low pressures the rise in T_e can hardly compensate for the reduction in pressure. The discharge cannot be sustained below a certain pressure value when function

$$f(T_e) = k_{ion}(T_e)/\sqrt{T_e}$$

has reached its maximum at ~50 eV. In the present experiment, the discharge extinguishes at ~0.006 Pa.

The technique employing ion/neutral line ratios have been also used in [9]. The authors normalize their results to the Langmuir probe measurements. They provide empirically obtained parameters for their (6) which computes the electron temperature for a given line ratio. One of the three line ratios in that work corresponds to our r_2. Hence, we can use our r_2 data to calculate T_e as recommended in [9]. This is shown with open circles in Fig. 5(a). The agreement is excellent throughout most of the pressure range.

It is important to emphasize that expression (1) was applied directly, without any adjustable parameters. We can refine our model and introduce a fit parameter, taking into account the fact that the creation of charged particles is determined by the volume-average $\overline{n_e}$, whereas the loss is controlled by the density at the sheath interface n_{es}. In doing so, d_{eff} must be multiplied with the ratio $\overline{n_e}/n_{es}$. A value around 1.3 of this parameter would improve on certain details in the pressure range below 0.02 Pa. Thus, the calculated pressure limit of discharge sustention is shifted to a somewhat lower value,

the agreement in T_e in Fig. 5(a) becomes better and the the relative electron density calculated from P_{abs} [Fig. 6(a)] matches better to those obtained with the other techniques. This is because $T_e(p)$ acquired with $\overline{n_e}/n_{es} = 1.3$ is lower than the one given in Fig. 5(a). The difference in magnitude is about 30% at $p = 0.01$ Pa and about 8% at $p = 0.1$ Pa. Apart from that, the results are not significantly changed.

The difference in absolute values of plasma density [see Fig. 6(b)] as calculated from the resonance magnetic field and from the absorbed power can be well explained by plasma nonuniformity. Regarding the radial profile of electron number density $n_e(r)$, the topology of the discharge ensures that the values are maximized on the symmetry axis and decrease toward the glass walls. While (6) gives value on the axis n_{e0}, the absorbed power in (7) is rather determined by an average value $\overline{n_e}$, which is lower. For example, an experimental profile $n_e(r)$ in [7] (see Fig. 2 therein) yields $n_{e0}/\overline{n_e} \approx 3.4$, which is to compare with the value 3.5 observed in our experiment. This agreement is strikingly good, bearing in mind that the power absorption is also highly nonuniform (as shown in simulations [19], [21]), which we neglected for simplicity. However, the regions of maximum power absorption are located between the center and the walls where $n_e(r) \approx \overline{n_e}$.

Typical values for n_{e0} found in the literature are about 10^{11} cm^{-3}, whereas it is of the order of 10^{10} cm^{-3} in our case. This is a consequence of the larger dimensions of our plasma source. The electron number density is inversely proportional to the plasma dimension squared, as is clear from (7) $n_e \sim S^{-1}$ or from (6) $n_e \sim l^{-2}$. As an example, l^{-2} in [8] is smaller by a factor of 5.4 than in our case, and consequently n_e is larger by the same factor (at a comparable P_{abs} magnitude).

With the input power being held constant, the variation of n_e with pressure is linked to the change in T_e and thus in ionization cost function $\mathcal{E}(T_e)$, which grows almost linearly at higher T_e.

Regarding the excited states' density, it does not go against expectations that $n_r \ll n_m$. Indeed, in our pressure range, the escape factor of the resonance line is about $\theta \sim 0.01$ [23], so the rate of radiative losses $\sim 10^6$ s^{-1} is about two orders of magnitude higher than all the other losses, making n_r lower then n_m by the same factor.

The behavior of the $1s_5$ number density can be modeled on the basis of the balance equation (see [24, eq. (3.27)]). Complete modeling is a challenging task, demanding to take into account the coupling to the kinetics of the other excited states, most notably that of the 1s and 2p-manifold, diffusion and collisions with the walls, consistent knowledge of all cross sections, and so on. This goes beyond the scope of the present study. Still, we can pose a meaningful question and try to answer it—what is the cause for the sharp increase of the metastable population at the lowest pressures, seen in Fig. 7?

Our quantitative estimations show that collisional-radiative coupling to the 2p-manifold plays a dominating role in both production and losses of the metastables. The production through the 2p-levels implies the cascades, caused by an excitation of a 2p-level from the ground state followed by its relaxation to the $1s_5$ state through a photon emission. Hence,

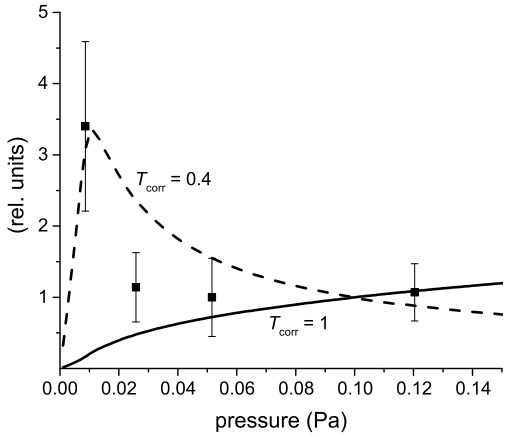

Fig. 10. Relative pressure dependece of the $1s_5$-state density (full squares) and of the calculated production/loss ratio according to (10) with $T_{corr} = 1$ (full line) and $T_{corr} = 0.4$ (dashed line).

one has to sum the optical excitation rate constants $k_{opt}^{s_5-p_x}$ for all the $1s_5$–2p spectral lines

$$k_{casc}^{2p} = \sum_{x=1}^{10} k_{opt}^{s_5-p_x}.$$

Population through the cascades is then given by $n_g n_e k_{casc}^{2p}$ and the largest individual contributions are provided by $2p_9, 2p_{10}, 2p_6, 2p_8$ states. The loss through the 2p-states starts with an electron impact excitation of the metastable state into a $2p_x$ level, followed by an optical relaxation to a state different from $1s_5$. The rate constant for such losses is therefore

$$k_{loss}^{2p} = \sum_{x=1}^{10} k_{s_5,p_x}(1 - b_{s_5,p_x})$$

with k_{s_5,p_x} being the rate constant of the excitation transfer to a given $2p_x$ state, and b_{s_5,p_x} the branching ratios giving the probability for a $2p_x$ state to radiatively decay into the $1s_5$ level. The major contributions are related to the $2p_8, 2p_6, 2p_{10}$ and $2p_3$ levels. While the electron impact cross section for the $1s_5 \rightarrow 2p_9$ excitation transfer is the largest [25], this pathway drops out completely due to the branching ratio $b_{s_5,p_9} = 1$, meaning that the radiative decay always brings a $2p_9$ atom back into the $1s_5$ state.

We can also take into consideration the direct ground state excitation k_{gm} as an additional production channel for the metastables. Then, in principle, the ratio of the production and the losses will reflect the behavior of the $1s_5$ state with varying plasma conditions

$$\frac{n_g n_e (k_{casc}^{2p}(T_e) + k_{gm}(T_e))}{n_e k_{loss}^{2p}(T_e)} = \frac{n_g k_{0,s5}(T_e)}{k_{loss}^{2p}(T_e)} \qquad (10)$$

where $k_{0,s5} = k_{casc}^{2p} + k_{gm}$ is the *apparent* excitation as it was designated by Donnelly [24].

This ratio is independent of n_e and can be computed as function of pressure employing the $T_e(p)$ curve found in Section IV-A. The result is plotted in Fig. 10 in solid line. This line monotonically approaches zero due to the multiplier

n_g in (10). The same ratio without n_g would manifest a peak at $p \sim 0.0135$ Pa. Even in product with n_g, this peak can be made visible when we reduce the absolute value of T_e used in the simulation, while keeping the same relative course. We can do it by variation of a scaling parameter T_{corr}: $T_e(p, T_{corr}) = T_{corr} T_e(p)$. Two calculated curves are compared in Fig. 10, the one with the original temperature curve $T_{corr} = 1$ and the other with $T_{corr} = 0.4$. The peak, associated with the 2p-cascades, is clearly seen in the latter case.

This could provide a good explanation for the experimental $1s_5$ density if it was not for the need to make the temperature that low. As pointed out earlier, a somewhat more refined charged particles balance model which makes distinction between volume-average $\overline{n_e}$ and the sheath interface n_{es} allows for a reduction of 30% in T_e at the lowest pressure. This is not enough to explain the reduction of 60% though. We can hypothesize that a change in the shape of the energy distribution function (EDF) of electrons becomes crucial at this low pressure. In any case, the effect of the maxwellizing electron–electron collisions is reduced as the pressure goes down, and variation in shape has been observed (see [3]). The production and destruction of the metastables by electron impact are controlled by different parts of the EDF, which would explain the need for an additional reduction of T_e within a Maxwellian-based model.

A theoretical 1-D kinetic model of the weakly magnetized discharge was proposed in [15]. The surface plasma impedance was also calculated there. We cannot directly compare the measured plasma resistance from Fig. 9(a) with the theoretical predictions due to the lack of experimental function $n_e(B_0)$. Nevertheless, the behavior of the resistance curve is similar. The position of the ECWR peak is at $\beta \approx 2$ for the lower p and therefore a lower n_e and is shifted to $\beta \approx 3$ at the higher p. This is well described by (6). The peak value of $\mathrm{Re}(Z)$ increases with increasing n_e, as it also follows from expression (40) in [15]. A small electron cyclotron resonance (ECR) peak at $\beta \sim 1$ or slightly above is present, although not always clearly seen. The presence of ambipolar potential makes the ECR peak observable in the first place (refer to Fig. 18 in [15]) and determines its exact position.

VI. Conclusion

In this paper, an ECWR plasma source is studied at very low pressures close to the limit of a sustained discharge. The electron temperature was high enough to observe Ar(II) lines and to use them for verification of $T_e(p)$ curve from the particle balance. In the end, the model was slightly refined to fit better to the observations. The electron density was also determined. It was somewhat lower than in earlier experiments at comparable power due to the large dimensions of our plasma source. The discharge was electrically characterized and the plasma resistance was reported for the first time in the literature.

Acknowledgment

The authors would like to thank C. Röthlein from Hiden Analytical for his friendly support during experiments.

References

[1] H.-J. Lee, I.-D. Yang, and K.-W. Whang, "The effects of magnetic fields on a planar inductively coupled argon plasma," *Plasma Sources Sci. Technol.*, vol. 5, no. 3, p. 383, 1996.

[2] C. W. Chung, S. S. Kim, and H. Y. Chang, "Electron cyclotron resonance in a weakly magnetized radio-frequency inductive discharge," *Phys. Rev. Lett.*, vol. 88, Feb. 2002, Art. no. 095002.

[3] V. A. Godyak and B. M. Alexandrovich, "Plasma and electrical characteristics of inductive discharge in a magnetic field," *Phys. Plasmas*, vol. 11, no. 7, pp. 3553–3560, 2004.

[4] Y.-D. Kim, Y.-K. Lee, H.-C. Lee, and C.-W. Chung, "Spatial measurements of electron energy distribution and plasma parameters in a weakly magnetized inductive discharge," *Phys. Plasmas*, vol. 20, no. 2, 2013, Art. no. 023505.

[5] W. H. Lee, H. W. Cheong, J. W. Kim, and K. W. Whang, "Improvement of uniformity in a weakly magnetized inductively coupled plasma," *Plasma Sources Sci. Technol.*, vol. 24, no. 6, 2015, Art. no. 065012.

[6] H. Oechsner, "Theoretical background and some applications of ECWR-plasmas," *Vacuum*, vol. 83, no. 4, pp. 727–731, Nov. 2008.

[7] E. P. Szuszczewicz, "On electron-cyclotron wave resonance in inductively coupled hf discharges," *J. Appl. Phys.*, vol. 42, no. 12, pp. 4794–4798, 1971.

[8] H. Oechsner, "Electron cyclotron wave resonances and power absorption effects in electrodeless low pressure h.f. plasmas with a superimposed static magnetic field," *Plasma Phys.*, vol. 16, no. 9, p. 835, 1974.

[9] G. Crolly, and H. Oechsner, "Comparative determination of the electron temperature in AR-and N_2-plasmas with electrostatic probes, optical emission spectroscopy OES and energy dispersive mass spectrometry EDMS," *Eur. Phys. J. Appl. Phys.*, vol. 15, no. 1, pp. 49–56, Jul. 2001.

[10] G. Franz, "Comprehensive analysis of chlorine-containing capacitively coupled plasmas," *J. Vacuum Sci. Technol. A*, vol. 23, no. 3, pp. 369–387, 2005.

[11] X.-M. Zhu and Y.-K. Pu, "Optical emission spectroscopy in low-temperature plasmas containing argon and nitrogen: Determination of the electron temperature and density by the line-ratio method," *J. Phys. D, Appl. Phys.*, vol. 43, no. 40, Sep. 2010, Art. no. 403001.

[12] M. A. Lieberman and A. J. Lichtenberg, *Principles of Plasma Discharges and Materials Processing*, 2nd ed. Hoboken, NJ, USA: Wiley, 2005.

[13] Á. Yanguas-Gil, J. Cotrino, and L. L. Alves, "An update of argon inelastic cross sections for plasma discharges," *J. Phys. D, Appl. Phys.*, vol. 38, no. 10, p. 1588, 2005.

[14] J. B. Boffard, B. Chiaro, T. Weber, and C. C. Lin, "Electron-impact excitation of argon: Optical emission cross sections in the range of 300–2500 nm," *At. Data Nucl. Data Tables*, vol. 93, no. 6, pp. 831–863, Nov. 2007.

[15] O. V. Polomarov, C. E. Theodosiou, I. D. Kaganovich, D. J. Economou, and B. N. Ramamurthi, "Self-consistent modeling of nonlocal inductively coupled plasmas," *IEEE Trans. Plasma Sci.*, vol. 34, no. 3, pp. 767–785, Jun. 2006.

[16] V. P. Sushkov, H. T. Do, and R. Hippler, "Application of the escape factor method for determination of excited states densities in a low-pressure argon radio-frequency discharge," *Contrib. Plasma Phys.*, vol. 53, no. 7, pp. 549–559, 2013.

[17] M. Schulze, A. Yanguas-Gil, A. von Keudell, and P. Awakowicz, "A robust method to measure metastable and resonant state densities from emission spectra in argon and argon-diluted low pressure plasmas," *J. Phys. D, Appl. Phys.*, vol. 41, no. 6, 2008, Art. no. 065206.

[18] S. Handelshauser, "Elektrische Impedanz eines ECWR Plasmas," B.S. thesis, Munich Univ. Appl. Sci., Munich, Germany, 2018.

[19] R. Krimke and H. M. Urbassek, "Calculation of electromagnetic fields and resonance conditions in a cylindrical ECWR discharge," *Plasma Sources Sci. Technol.*, vol. 6, no. 3, p. 415, 1997.

[20] V. Sushkov, A.-P. Herrendorf, and R. Hippler, "Metastable argon atom density in complex argon/acetylene plasmas determined by means of optical absorption and emission spectroscopy," *J. Phys. D, Appl. Phys.*, vol. 49, no. 42, 2016, Art. no. 425201.

[21] S. Sfikas, E. Amanatides, D. Mataras, and D. Rapakoulias, "Simulation of cylindrical electron cyclotron wave resonance argon discharges," *J. Phys. D, Appl. Phys.*, vol. 44, no. 16, 2011, Art. no. 165204.

[22] R. Hippler, J. Kredl, and V. Vartolomei, "Ion energy distribution of an inductively coupled radiofrequency discharge in argon and oxygen," *Vacuum*, vol. 83, no. 4, pp. 732–737, 2008.

[23] C. M. Ferreira, J. Loureiro, and A. Ricard, "Populations in the metastable and the resonance levels of argon and stepwise ionization effects in a low-pressure argon positive column," *J. Appl. Phys.*, vol. 57, no. 1, pp. 82–90, 1985.
[24] V. M. Donnelly, "Plasma electron temperatures and electron energy distributions measured by trace rare gases optical emission spectroscopy," *J. Phys. D, Appl. Phys.*, vol. 37, no. 19, p. R217, 2004.
[25] K. Bartschat and V. Zeman, "Electron-impact excitation from the ($3p^5 4s$) metastable states of argon," *Phys. Rev. A*, vol. 59, p. R2552, Apr. 1999.

Vladimir P. Sushkov received the master's degree in physics from St. Petersburg State University, St. Petersburg, Russia, in 2003, and the Ph.D. degree in plasma physics from the University of Greifswald, Greifswald, Germany, in 2014.

Since 2016, he has been a Post-Doctoral Fellow with the Munich University of Applied Sciences, Munich, Germany. His current research interests include optical spectroscopy, plasma diagnostics, and discharge modeling.

Severin A. Handelshauser received his bachelor's degree in engineering physics from the Munich University of Applied Sciences, Munich, Germany, in 2018.

In 2018, he moved to the Ludwig Maximilian University of Munich to complete his master's studies. His current research interests include the capabilities of modern physics and technology.

Gerhard Franz received the master's degree in physical chemistry from Philipps University, Marburg, Germany, in 1977, and the Ph.D. degree, with a thesis on the thermodynamical and conductivity aspects of the fluid alkali metals rubidium and cesium up to their critical point, from Philipps University, in 1980.

In 1981, he joined the Analytical Department, Siemens Research Laboratories, Munich, Germany. In 1986, he moved to the Photonics Department, Siemens Research Laboratories, where he became responsible for the development of plasma-based processes in 1992. In 2002, he joined the Munich University of Applied Sciences, Munich, where he is currently a Professor of applied physics. In 2005, he founded the Center for Nanostructure Technology together with some colleagues from the Technical University of Munich, Munich. He has authored or coauthored four books on low-temperature plasma physics and microstructuring technology and more than 60 peer-reviewed papers (among which are 14 one-author papers and 13 first-author papers) and has given more than 70 external lectures.

Dr. Franz has been a member of the American Vacuum Society since 1997.